



www.sciencemag.org/cgi/content/full/329/5989/316/DC1

Supporting Online Material for

**Cenozoic Tectonics of Western North America Controlled by Evolving
Width of Farallon Slab**

W. P. Schellart,* D. R. Stegman, R. J. Farrington, J. Freeman, L. Moresi

*To whom correspondence should be addressed. E-mail: wouter.schellart@monash.edu

Published 16 July 2010, *Science* **329**, 316 (2010)

DOI: 10.1126/science.1190366

This PDF file includes:

Materials and Methods

Figs. S1 to S3

Table S1

References

SUPPORTING ONLINE MATERIAL

CENOZOIC TECTONICS OF WESTERN NORTH AMERICA CONTROLLED BY EVOLVING WIDTH OF FARALLON SLAB

W.P. Schellart^{1*}, D.R. Stegman^{2,3}, R.J. Farrington⁴, J. Freeman^{4,5}, L. Moresi^{1,4}

¹*School of Geosciences, Monash University, Melbourne, VIC 3800, Australia*

²*Scripps Institution of Oceanography, University of California, San Diego, La Jolla, CA 92093,
USA*

³*School of Earth Sciences, University of Melbourne, Melbourne, VIC 3010, Australia*

⁴*School of Mathematical Sciences, Monash University, Melbourne, VIC 3800, Australia*

⁵*Bureau of Meteorology, Melbourne, VIC 3001, Australia*

***Corresponding author**

W. P. Schellart
School of Geosciences
Monash University
Melbourne VIC 3800
AUSTRALIA

Phone: +61 3 9905 1782
Fax: +61 3 9905 4903
Email: wouter.schellart@monash.edu

1. Methods

1.1. Numerical method

Subduction and plate motion are modeled in a three-dimensional Cartesian box by chemical convection in an incompressible Boussinesq fluid at infinite Prandtl number and very low Reynolds number. A dense high-viscosity plate (subducting oceanic lithosphere) overlies a less dense low-viscosity volume (sub-lithospheric mantle) (Fig. S1).

The nondimensional equations describing the flow in the models and details on the numerical technique are described elsewhere (S1, S2). The numerical model design is based on earlier work (S1, S3), but has been significantly improved in that the subducting plate has four layers (each 25 km thick) instead of only one or two. The plate includes a relatively strong viscous core, following Capitanio et al. (S4, S5) and Ozbench et al. (S6), resulting in plate-like behavior of the surface plate and efficient slab-plate coupling. The plate has a viscoplastic top layer (maximum viscosity of 1000 times that of the upper mantle, η_{UM}) followed by 3 linear-viscous layers with a progressively decreasing viscosity ($300\eta_{UM}$, $50\eta_{UM}$ and $10\eta_{UM}$). The effective viscosity of the slab is thus $\sim 10^2 \times \eta_{UM}$, closely reflecting effective viscosity ratios between slab and upper mantle as deduced previously for the natural prototype ($1-3 \times 10^2$) (S5, S7-S14).

The viscosity of the uppermost viscoplastic part of the plate is represented by an effective viscosity:

$$\eta_{\text{eff}} = \min[\eta_0, \eta_y] \quad (1)$$

where the plastic branch of the rheology, η_y , is defined as:

$$\eta_y = \frac{\tau_y}{2\dot{\epsilon}_{II}} \quad (2)$$

with

$$\dot{\epsilon}_{II} = \sqrt{\frac{1}{2} \dot{\epsilon}_{ij} \dot{\epsilon}_{ij}} \quad (3)$$

and

$$\dot{\epsilon}_{ij} = \frac{1}{2} \left(\frac{\partial u_i}{\partial x_j} + \frac{\partial u_j}{\partial x_i} \right) \quad (4)$$

and the isotropic yield stress, τ_y , is given by:

$$\tau_y = \tau_0 \quad (5)$$

where τ_0 is the cohesive strength (equivalent to 48 MPa in nature) (S15, S1). The yield stress represents a parameterization of the sub-scale physics occurring within the subduction hinge (i.e. a set of unresolved normal faults that develop during plate bending). The relevant value for yield stress is highly uncertain, but lies somewhere between the maximum stress supported by pre-existing faults and the stress required to produce faulting in weakened (and possibly serpentized) rocks. τ_y represents a von Mises yield function and is chosen such that the resultant effective viscosity matches observations of slab strength in the upper mantle. This effective viscosity is also consistent with current estimates of bending resistance at the plate's hinge (S14, S5). The models have a slab and trailing plate that remain coupled, show trenchward

subducting plate motion and exhibited very low strain rates in the trailing plate for the duration of the experiment (Figs. S2 and S3). This is also observed in laboratory models of subduction (S16, S17, S9, S10).

The velocities in the models (v') were scaled to velocities on Earth (v) following:

$$v = v'(\eta'_{UM}\Delta\rho g T_{SP} T_{UM})/(\eta_{UM}\Delta\rho' g' T_{SP}' T_{UM}') \quad (6)$$

where $\Delta\rho$ is the density contrast between the subducting plate and upper mantle (80 kg/m^3), g is the gravitational acceleration (9.8 m/s^2), T_{SP} is the subducting plate thickness (100 km), T_{UM} is the upper mantle thickness (660 km) and η_{UM} is the upper mantle dynamic viscosity ($1.57 \times 10^{20} \text{ Pa}\cdot\text{s}$).

In the interest of simplicity, we do not consider the effects of thermal diffusion nor the presence of an overriding plate, following previous work (S1, S3-S6, S16-S18). Thus, the single plate subducts in isolation and is not affected by mantle flow induced by neighboring slabs or large-scale mantle flow. The exclusion of an overriding plate is justified as a first-order approximation, because a recent global statistical investigation indicates that the subducted slab predominantly determines the trench velocity, whilst the role of the overriding plate in determining the trench velocity is of subordinate importance (S19). Due to the absence of an overriding plate, the subduction fault has the same viscosity as the ambient upper mantle. Although this is a low strength, global considerations (S15) and regional studies (S20-S22) imply that the subduction fault is very weak. Such a low strength further implies that the subduction fault does not control the subduction velocity, again indicating that our simplification of overriding plate exclusion is justified as a first-order approximation.

The plate is laterally homogeneous and has a thickness representing 100 km in nature, corresponding to mature oceanic lithosphere ($\geq 80 \text{ Ma}$) with a density contrast of 80 kg/m^3 with respect to the underlying mantle. The density contrast of 80 kg/m^3 was based on the detailed study from Cloos (S23), who calculated that for an 80 million year old 100 km thick oceanic lithosphere, including a 7 km thick basaltic crust, the average density contrast between slab and ambient mantle is 40 kg/m^3 , where the lithospheric mantle contributes a negative, thermal, buoyancy and the crust contributes a positive compositional buoyancy because it is relatively light ($\sim 2900 \text{ kg/m}^3$). Additional negative buoyancy results from metamorphism of the basaltic crust into dense eclogite facies rocks ($\sim 3400 \text{ kg/m}^3$), and the average density contrast between subducted slab and ambient mantle is then 80 kg/m^3 (S23). The eclogitization starts at a depth of $\sim 40 \text{ km}$, implying that for almost the entire upper mantle slab, the crust will consist of dense eclogite facies rocks. Recent numerical work from Afonso et al. (S24) implies that a 100 km thick 90 Ma oceanic lithosphere, including a 7 km thick basaltic crust (2900 kg/m^3), has a somewhat smaller average density contrast with the asthenosphere of 35.5 kg/m^3 , in which the mantle lithosphere has a density contrast of 63.4 kg/m^3 and the crust has a density contrast of -335 kg/m^3 . Assuming again that, upon subduction, the crust is metamorphosed into eclogite facies rocks, then the average density contrast between slab and ambient mantle will be 70.5 kg/m^3 . This value is comparable to the 80 kg/m^3 from Cloos (S23). In this study we adopt a density contrast of 80 kg/m^3 .

Due to geometrical symmetry with respect to the mid-plane of the subduction zone and due to the low Reynolds number, all experiments were run in a Cartesian box with only half the dimension in the trench-parallel direction. Plates have an initial length of 2200 km of flat-lying lithosphere with an additional slab length of 187 km dipping at 15.5° to initiate progressive

subduction. Slab width (W), i.e. its trench-parallel extent, varies for successive experiments between 300 and 7,000 km, while box size is constant (see Table S1). In all experiments, separation between lateral slab edge and lateral sidewall is always $\geq 0.5W$, separation between the trench and front wall is always $\geq 0.5W$ and velocity boundary conditions are free-slip everywhere to minimize influence of the box sidewalls. In all simulations the box is large enough such that no appreciable amount of deformation occurs on the sidewalls (Fig. S3), which verifies that the side-wall boundary conditions are not influencing the subduction dynamics or the induced flow significantly.

A free trailing edge boundary condition is applied to the plate and represents Pacific style subducting plates with a spreading ridge at their trailing edge (S25). The upper/lower mantle transition is represented as a viscosity discontinuity at a depth of 660 km. The lower mantle is significantly more viscous than the upper mantle, and estimates range between a factor of 10^1 and 10^3 (S26, S27). We apply a viscosity jump of a factor of 10^2 between the upper and lower mantle and choose a linear viscous rheology for the entire sublithospheric mantle. The simple implementation of the viscosity jump incorporates all the effects of the 660 km phase transition (viscosity changes, density changes and thermodynamic reactions from mineral phase transition) and captures the fluid dynamic essence of this barrier by reducing the sinking velocity of slabs in the lower mantle, as indeed implied by recent numerical work on phase transitions and deep mantle mineral physics (S28, S29). In all models, the mantle is 1,000 km deep with 340 km of high-viscosity lower mantle. The effect of the bottom boundary was tested by comparing a 1,000 km deep model (340 km lower mantle) with a 2,000 km deep model (1,340 km lower mantle) (S3). It was found that the trench migration velocity and plate kinematics were nearly identical in both runs, implying that the bottom boundary is not influencing the results significantly.

1.2. Kinematic calculations

The trench-normal subducting plate velocity ($v_{SP\perp}$), trench-normal trench migration velocity ($v_{T\perp}$) and subduction partitioning ($v_{SP\perp}/v_{S\perp}$) were calculated for all major subduction zones on Earth (24 in total). The convention is that trenchward subducting plate motion and retrograde (oceanward) trench motion (i.e. trench retreat) are positive. With these conventions, then $0 < v_{SP\perp}/v_{S\perp} < 1$ with both trenchward subducting plate motion and trench retreat, $v_{SP\perp}/v_{S\perp} > 1$ with trenchward subducting plate motion and trench advance, and $v_{SP\perp}/v_{S\perp} < 0$ with oceanward subducting plate motion and trench retreat. The trench velocity and subduction velocity were calculated as follows:

$$v_{T\perp} = v_{OP\perp} + v_{OPD\perp} + v_{A\perp} \quad (7)$$

and

$$v_{S\perp} = v_{SP\perp} + v_{T\perp} \quad (8)$$

where $v_{OP\perp}$ is the trench-normal overriding plate (+ potential microplate) velocity (trenchward velocity is positive), $v_{OPD\perp}$ is the trench-normal overriding plate deformation rate (i.e. fore-arc, intra-arc or backarc extension/shortening; extension is positive, shortening is negative), and $v_{A\perp}$ is the trench-normal trench accretion/erosion rate (accretion is positive, erosion is negative). More details on the calculations of $v_{T\perp}$ and $v_{SP\perp}$ are presented elsewhere (S30, S31). The trench accretion/erosion rates for individual subduction zones were derived primarily from (S32).

Each of the 24 subduction zones was subdivided into 200 km trench segments (total of 244 segments). The choice for this length scale was based on the rationale that it should exceed the thickness of old oceanic lithosphere (so $> \sim 100$ km), but should not exceed the width of the narrowest subduction zone (so $< \sim 250$ km). Subduction zone segments for which the subduction velocity $v_{s\perp} \leq 1.5$ cm/yr, as well as all segments of a particular subduction zone for which the average $v_{s\perp} \leq 1.5$ cm/yr, were excluded from the calculations. For this reason, 17 subduction zones are plotted in Figs. 1B-C and Figs. 2A-C in the paper using a total of 207 trench segments, while 7 subduction zones were not included (Betic-Rif, Cyprus, Puysegur, Sangihe, Trobriand, Venezuela, Lesser Antilles-Puerto Rico). The average values for individual subduction zones/plates as plotted in Figs. 1 and 2A-C were calculated from the number of trench segments in each of these subduction zones/plates.

For the numerical models, the velocities for the 11 experiments plotted in Figs. 2D-F were also averaged over the entire subduction zone extent. The experiments started with a short subduction instability (187 km long slab dipping at 15.5°) and ran until the trench reached the trailing edge of the plate within 100-200 km, or when the entire plate was subducted. Each experiment lasted some 26-30 Myr and kinematic data were extracted for the subduction phase between 8 Myr and 24-27 Myr. For each experiment, the last 2-4 Myr were excluded from the calculations because the trench would get within ~ 200 km of the trailing edge and the plate started to become unstable as a whole, resulting in unsteady plate and trench velocities. In addition, we excluded the first 8 Myr of subduction from the calculations (the incipient subduction stage), during which the average depth of the slab tip was ~ 300 km, slab sinking was mostly accelerating and the subduction velocity $v_{s\perp} \leq 1.5$ cm/yr for most of this first period. We have excluded these first 8 Myr because the natural subduction zones that are included in Figs. 2A-C are all in an advanced subduction stage (except maybe South Shetland), for which the slabs have reached a depth of either ~ 500 km (e.g. Aleutians, Ryukyu, New Hebrides), have reached the transition zone (~ 660 km, e.g. Scotia, New Britain), are flattened at on the transition zone (e.g. Tonga, Japan, Izu-Bonin, Calabria), or have penetrated into the lower mantle (e.g. Hellenic, Mariana, Central America). As such, the 17 different subduction zones that are plotted in Figs. 2A-C are in an advanced stage of their evolution that is replicated in the models for the period 8 Myr to 24-27 Myr. As such, the comparison between natural subduction zones and experimental subduction zones as presented in Fig. 2 is justified.

Plate velocities and plate boundary velocities in nature depend on the choice of global reference frame (S30). For the data presented in Figs. 1 and 2 in the paper we use the Indo-Atlantic moving hotspot reference frame (S33) because: (1) it is a recent global reference frame that incorporates the slow relative motions of the hotspots; (2) it minimizes global viscous dissipation in the mantle (S30); (3) the net rotation of the lithosphere in this reference frame is in accordance with predictions from spherical convection models and observed anisotropy patterns in the mantle (S34); and (4) it can account for V-shaped fracture segments that link across the spreading ridge segments in the Atlantic (S35). Calculations in several other global reference frames such as a global fixed hotspot reference frame (S36), a geophysical no-net-rotation reference frame (S37), a geodetic no-net-rotation reference frame (S38) and a Pacific fixed hotspot reference frame (S39) give comparable trends for $v_{SP\perp}$, $v_{T\perp}$ and $v_{SP\perp}/v_{S\perp}$, although maximum discrepancies can be up to 2-3 cm/yr.

As mentioned in the previous paragraph, we use the Indo-Atlantic moving hotspot reference frame (S33). In addition, we use a geophysical relative plate motion model (S40) and mainly geological/geophysical overriding plate deformation rates. Error margins for $v_{SP\perp}$, $v_{T\perp}$ and $v_{SP\perp}/v_{S\perp}$

are very hard to quantify. In particular, error margins for $v_{T\perp}$ cannot be quantified, simply because the calculations for individual segments are based on a large variety of source material, for which error estimates are often not provided. Trench velocity is calculated from the overriding plate velocity in a particular reference frame, from the overriding plate deformation rate and from the accretion/erosion rate at the trench [see equation (7)]. Overriding plate deformation rate estimates based on geophysical or geological studies often do not come with uncertainties. Also, the trench accretion/erosion rates do not come with uncertainty estimates, but these rates are generally rather small (few mm/yr), so their errors are probably also small. A rough estimate of the errors due to uncertainty in backarc deformation rates and trench accretion/erosion rates would amount up to a maximum of ~ 1 cm/yr. Finally, the largest source of uncertainty in “absolute” trench and plate velocities is the choice of global reference frame, with up to several cm/yr of variation [see for example discussion in Schellart et al. (S30)]. Our justification for using the Indo-Atlantic moving hotspot reference frame is detailed in the previous paragraph.

Values for fraction of plate boundary attached to a subducting slab as presented in Fig. 1A are calculated predominantly from the plate tectonic model from Bird (S41). Average ages for subducting oceanic lithosphere as presented in Figs. 1B and 1C in the manuscript are compiled from the database presented in (S31) and represent the average age at the trench. Ages are well determined for most subduction zones and uncertainties in average age are therefore relatively small and not more than about $\pm 10\%$, except for Makran with an uncertainty of about $\pm 20\%$ (75 Ma ± 15 million years) and Calabria and Hellenic with an uncertainty of about $\pm 30\%$ (140 Ma ± 40 million years).

For the diagrams presented in Fig. 3 in the paper we use the global plate motion model from Gordon and Jurdy (S36), which makes use of a global hotspot reference frame. The potential errors in the plate velocities most likely increase as one goes further back in time, estimated at up to ~ 1 cm at 60 Ma due to errors in the accuracy of the relative plate motion model, and an additional, larger, error due to uncertainties associated with the choice of reference frame. It is, however, very encouraging that preliminary investigations on the velocity of the Farallon plate, using the global plate motion model from Müller et al. (S42), which makes use of an Indo-Atlantic hotspot reference frame, show results that agree very well with those presented in Fig. 3B in the paper. Maximum average Farallon plate velocities of $v_{SP\perp} = 10$ -11 cm/yr occur at 60-40 Ma in the Müller et al. model, decreasing to ~ 6 cm/yr at 40-20 Ma, further decreasing to ~ 4 cm/yr at 20-10 Ma, and finally decreasing to ~ 2 cm/yr at 10-0 Ma. A very similar trend is observed in the Gordon and Jurdy model, with velocities gradually decreasing from 9-10 cm/yr at 56-43 Ma to ~ 2 cm/yr at 10-0 Ma (Fig. 3B). As such, we conclude that our finding of a general deceleration of the Farallon plate during the Cenozoic is robust.

2. Scaling formulations for slab width

2.1. Subducting plate velocity

The trench-normal subducting plate velocity ($v_{SP\perp}$) can be approximated with the formulation for Stokes-like sinking (v_{SINK}) of an oblate ellipsoid (cf. slab) parallel to its flat plane as described in Kerr and Lister (S43):

$$v_{SINK} = S\Delta\rho g(abc)^{2/3}/18\eta \quad (9)$$

where S is the shape factor ($S43$), $\Delta\rho$ is the density contrast between object and ambient fluid, g is the gravitational acceleration (9.8 m/s^2), a , b and c are the three principal axes of the ellipsoid, and η is the viscosity of the ambient fluid. With the assumption that $v_{\text{SP}\perp}$ translates to slab-dip-parallel motion at depth, then $v_{\text{SP}\perp} = c_{\text{SP}}v_{\text{SINK}}$, where c_{SP} is a constant ($c_{\text{SP}} \leq 1$) that depends in particular on the slab dip angle. We can further substitute the principal axes of the ellipsoid with the slab dimensions T (thickness), L (length, down-dip extent) and W (width, trench-parallel extent), and use a mantle viscosity that is in between that of the upper mantle and the lower mantle ($c_{\text{UM}}\eta_{\text{UM}}$, where $1 < c_{\text{UM}} < 100$). With $c_{\text{UM}}/c_{\text{SP}} = c_1$, this results in:

$$v_{\text{SP}\perp} = S\Delta\rho g(TLW)^{2/3}/18c_1\eta_{\text{UM}} \quad (10)$$

From equation (10) it can be seen that the subducting plate velocity scales with slab width as such: $v_{\text{SP}\perp} = k_1(W)^{2/3}$, with $k_1 = S\Delta\rho g(LT)^{2/3}/18c_1\eta_{\text{UM}}$. For the natural subduction zones we use the values for W as measured for the individual subduction zones (see key in Fig. 2) and for the numerical models we use the time-weighted mean W for each individual subduction experiment. The value of k_1 has been optimised for the best-fit non-linear curves as plotted in Figs. 2A and 2D. For this optimal fit we find that $k_1(\text{nature}) = 0.520 \times 10^{-12} - 0.993 \times 10^{-12}$ and $k_1(\text{models}) = 0.626 \times 10^{-12} - 1.109 \times 10^{-12}$. The minor variation in $k_1(\text{nature})$ and $k_1(\text{models})$ originates from variation in the shape factor S , which ranges between 0.49 and 0.94 (nature) and 0.55 and 0.97 (models), as derived from Kerr and Lister ($S43$). The shape factor itself varies because of variation in W . The minor difference between $k_1(\text{nature})$ and $k_1(\text{models})$ is because we choose $T = 100 \text{ km}$ for the natural subduction zones, while we use the time-weighted average for all subduction zones ($T = 113 \text{ km}$) for the numerical models. For the other parameters we have (for both nature and models) $\Delta\rho = 80 \text{ kg/m}^3$, $g = 9.8 \text{ m/s}^2$, $L = 600 \text{ km}$, $c_1 = 4.025$ and $\eta_{\text{UM}} = 1.57 \times 10^{20} \text{ Pa}\cdot\text{s}$.

2.2. Trench migration velocity

Trench-normal trench migration and associated lateral slab migration through the upper mantle require a mantle return flow from one side of the slab to the other side due to conservation of volume. This return flow occurs in a quasi-toroidal fashion and occurs exclusively around the lateral slab edges ($S1$, $S3$, $S9$, $S16$). The driving force for such quasi-toroidal flow originates from the potential energy of the negatively buoyant slab, $E_p(\text{slab})$. The viscous resistance to such flow originates from viscous drag of the ambient upper mantle at the slab-mantle interface, and viscous drag of the upper mantle at the upper-lower mantle discontinuity, which is defined by a strong viscosity step. The viscous dissipation due to viscous drag on the slab surface area [$\Phi_{\text{DRAG}}(\text{slab})$] scales with the slab surface area, while the viscous dissipation related to the viscous drag at the upper-lower mantle discontinuity [$\Phi_{\text{DRAG}}(\text{transition zone})$] scales with the plan-view extent of the toroidal flow patterns. The energy source and energy sinks thus relate as follows:

$$c_p E_p(\text{slab}) = \Phi_{\text{DRAG}}(\text{slab}) + \Phi_{\text{DRAG}}(\text{transition zone}) \quad (11)$$

where c_p is a constant with $c_p < 1$, because only part of the available potential energy is dissipated in $\Phi_{\text{DRAG}}(\text{slab}) + \Phi_{\text{DRAG}}(\text{transition zone})$. The potential energy of the upper mantle slab is simply related to the density contrast between slab and ambient upper mantle ($\Delta\rho$), the thickness of the upper mantle (z_{UM}), and the volume of the upper mantle slab, LWT , where L , W and T are the

length, width (trench-parallel extent) and thickness of the slab, respectively. The viscous dissipation due to drag on the slab is proportional to the surface area of the slab, the upper mantle viscosity (η_{UM}) and the trench-normal trench velocity ($v_{T\perp}$). The viscous dissipation due to the viscous drag at the upper-lower mantle transition zone resulting from the toroidal-type upper mantle return flow is proportional to η_{UM} , $v_{T\perp}$, and the lateral dimensions of the toroidal mantle return flow, which is approximately circular in plan view [see for example Schellart (S9) Fig. 12] and scales with $2\pi(W/2)^2$, with $W/2$ being the approximate radius of the circular flow pattern. Also note that there are two toroidal flow cells, one on each side of the symmetry plane through the centre of the subduction zone. We can now write the following:

$$c_P \Delta \rho g L W T z_{UM} \approx \eta_{UM} v_{T\perp} \left(c_S (2LW + 2LT) + 2c_T \pi (\frac{1}{2}W)^2 \right) \quad (12)$$

Rearranging equation (12) in terms of $v_{T\perp}$, and assuming that for the constants $c_S = c_T$ and that $c_2 = c_P/c_S$, results in:

$$v_{T\perp} \approx \frac{c_2 \Delta \rho g L T z_{UM}}{\pi \eta_{UM} \left(\frac{W}{2} + \frac{2L}{\pi} + \frac{2LT}{\pi W} \right)} \quad (13)$$

From equation (13) it follows that the trench-normal trench velocity is approximately inversely dependent on W : $v_{T\perp} \approx k_2/(W+k_3)$, with $k_2 = 2c_2 \Delta \rho g L T z_{UM}/\pi \eta_{UM}$ and $k_3 = (4L/\pi)(1+T/W)$. The third term in between the brackets in the denominator of equation (13) is only significant in case the slab width becomes relatively small ($W \leq L$). The value of k_2 has been optimised for the best-fit non-linear curves as plotted in Figs. 2B and 2E with $c_2 = 0.022$ and $z_{UM} = 660$ km, so $k_2(\text{nature}) = 0.0028$ and $k_2(\text{models}) = 0.0031$. For k_3 we use the average values of T , W and L as input. For both natural subduction zones and numerical models we have $L = 600$ km, for the natural subduction zones we have $T = 100$ km, for the numerical models we use the average T as calculated for all the subduction models as averaged over time with $T = 113$ km. For the natural subduction zones we use the values for W as measured for the individual subduction zones (see key in Fig. 2) and for the numerical models we use the time-weighted mean W for each individual subduction experiment.

3. Scaling formulations for slab age

To calculate the non-linear best-fit curves for trench-normal subducting plate velocity ($v_{SP\perp}$) and trench-normal trench velocity ($v_{T\perp}$) in Figs. 1B-C we use the same equation for Stokes sinking of a square upper mantle slab ($L = W$) as used by Goes et al. (S18) and Capitanio et al. (S4):

$$v_{Stokes} = \frac{TL^2 \Delta \rho g}{12\sqrt{2}L\eta_{UM}} \quad (14)$$

where T and L are the slab thickness and slab length, respectively; $\Delta \rho$ is the density contrast between slab and ambient mantle, g is the gravitational acceleration (9.8 m/s^2); and η_{UM} is the upper mantle viscosity. Following Goes et al. (S18) we assume that v_{STOKES} in equation (14) is

mainly dependent on the age of the slab and we thus let T and $\Delta\rho$ vary with age, following Cloos (S23), while fixing L ($= W$) at 1000 km. In Cloos (S23) T varies following a square root age law, while $\Delta\rho$ has both a thermal component and a chemical component (due to metamorphism of basalt into much denser eclogite). Finally, we assume that $v_{SP} \approx v_{Stokes}$, again following (S18), and that $v_T \approx a v_{Stokes}$, where a is a best-fit constant.

4. Calculations for Cenozoic Farallon plate subduction

We used the global Cenozoic plate reconstructions from Gordon and Jurdy (S36) to calculate the Cenozoic kinematic evolution of the Farallon plate (i.e. $v_{SP\perp}$), the kinematic evolution of the overriding plate(s) (North American plate and South American plate) (i.e. $v_{OP\perp}$), and the average age of the Farallon slab at the trench. The trench-parallel extent of the Farallon slab and the geometry of the Farallon plate, and as such the percentage of the Farallon plate boundary attached to downgoing oceanic lithosphere, were calculated using several works (S36, S44-S46). To calculate $v_{T\perp}$ we used $v_{OP\perp}$ for the North American plate and South American plate until 43 Ma and $v_{OP\perp}$ for the North American plate from 43 Ma to Present using the plate motion model in (S36), overriding plate shortening rates in North America from DeCelles (S45), overriding plate extension rates in the Basin and Range region from Sonder and Jones (S46), overriding plate extension rates in the Omineca extensional zone from Parrish et al. (S47), overriding plate shortening rates in South America from Oncken et al. (S48), and trench accretion/erosion rates along the North American and South American subduction zones from Clift and Vannucchi (S32). The extent of Sevier and Laramide shortening is from DeCelles (S45), while the extent of Basin and Range extension is from Sonder and Jones (S46) and Henry and Aranda-Gomez (S49). The subducting plate age at the trench for the data points in the period 60-5 Ma was estimated with the formula $Age = L_p/v_{SP\perp}$ for individual 400-2,000 km trench segments (where L_p is the local average ridge-trench distance and $v_{SP\perp}$ is averaged for the trench segment). We then averaged the subducting plate age for the entire subduction zone. For the Present day slab age at the trench we used the Juan de Fuca plate age map from Wilson (S50).

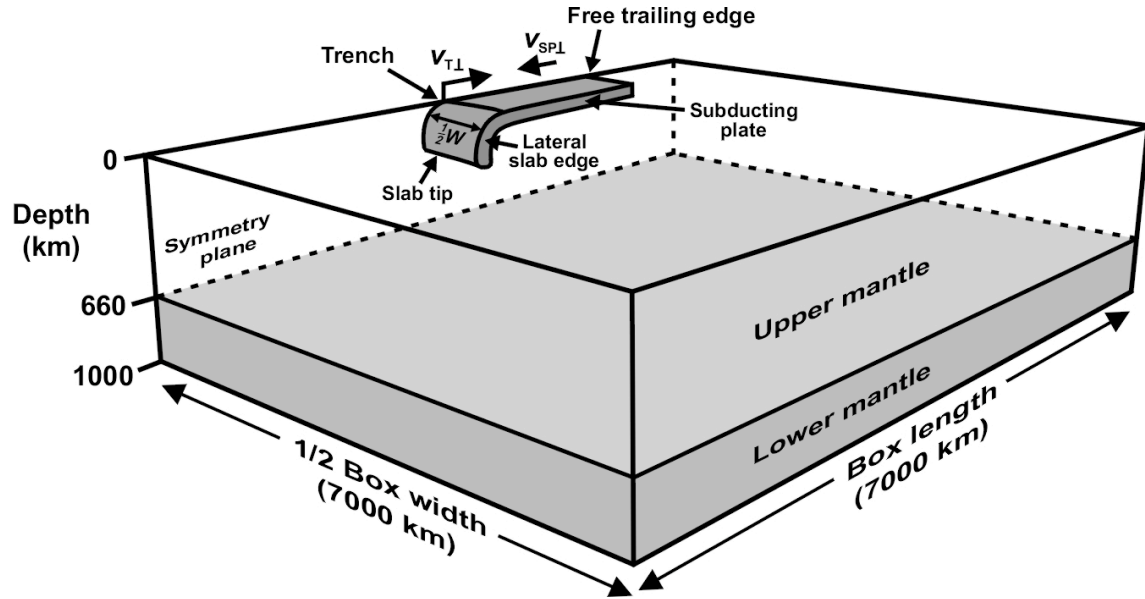


Figure S1. Numerical model configuration, showing a dense high-viscosity plate (representing mature oceanic lithosphere) overlying a lower-density layered linear viscous mantle, with a low viscosity upper mantle (η_{UM}) and an intermediate viscosity lower mantle ($100\eta_{UM}$), confined in a 3D Cartesian box. The plate is 100 km thick and consists of four 25-km-thick layers, with a viscoplastic top layer (maximum viscosity of $1000\eta_{UM}$) followed by three linear-viscous layers with decreasing viscosity from top to bottom ($300\eta_{UM}$, $50\eta_{UM}$ and $10\eta_{UM}$). The upper mantle is 660 km thick and is underlain by 340 km of lower mantle. Subduction is driven by buoyancy forces only, reflecting natural subduction systems. W indicates slab width, which is varied for each simulation (see Table S1). Each experiment starts with a 187 km long slab perturbation dipping at 15.5° . Note that only half of the model domain is shown (and calculated), because the experiment is symmetrical with respect to a plane through the centre of the subduction zone (symmetry plane in the figure). Details on the numerical method are described in the Methods section 1.1 and in previous work (S1, S2).

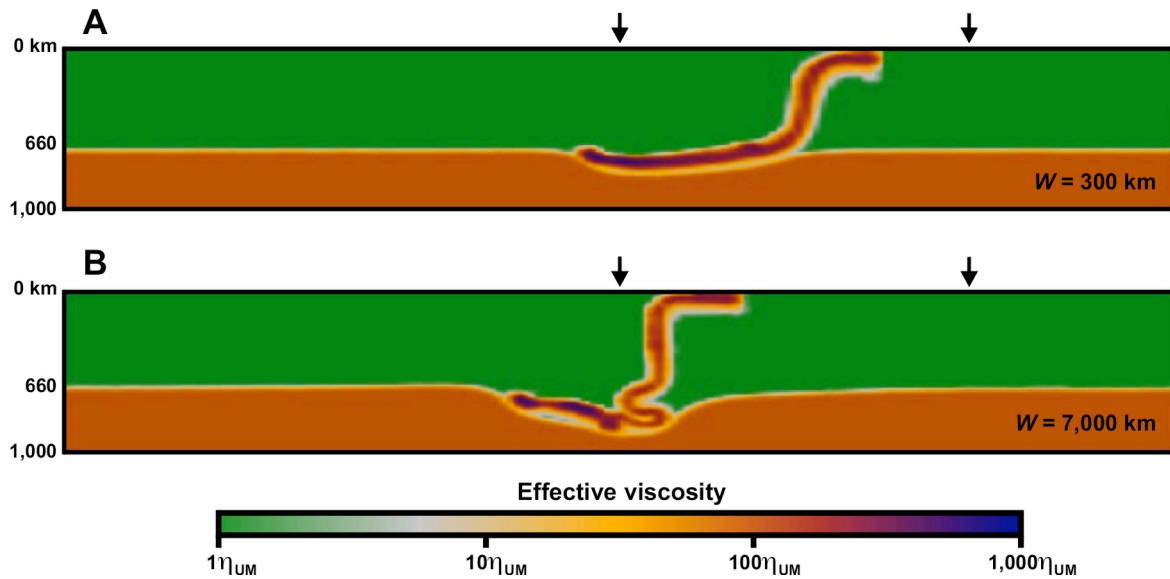


Figure S2. Cross-sections through the centre of the subduction zone in an advanced stage of subduction illustrating slab morphology and viscosity distribution for **(A)** a narrow-slab subduction experiment ($W = 300$ km), and **(B)** a wide-slab subduction experiment ($W = 7,000$ km). Subduction is driven by buoyancy forces only, reflecting natural subduction systems. As can be observed in the viscosity plots, the slab remains coupled to the trailing plate, thereby driving plate motion, whilst the trailing plate shows plate-like behavior. Arrows indicate initial position of the trench (arrows on the left) and trailing plate edge (arrows on the right). Note that the narrow slab is characterized by considerable trench retreat and minor plate advance, while the wide slab is characterized by minor trench retreat and considerable plate advance.

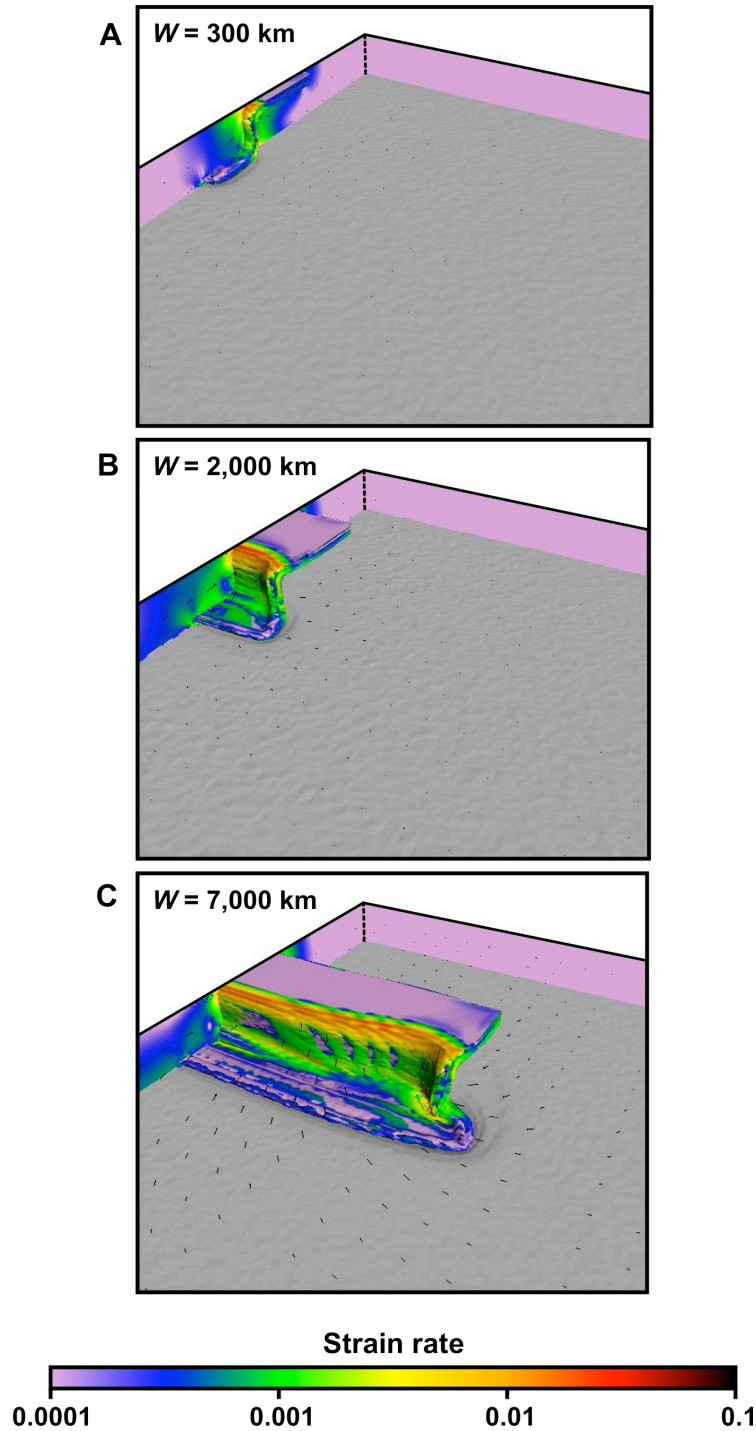


Figure S3. Three-dimensional perspective views of the subduction models in an advanced stage of subduction illustrating the low strain rates in the surface plate and at the back wall of the box for (A) a narrow slab ($W = 300 \text{ km}$), (B) an intermediate width slab ($W = 2,000 \text{ km}$), and (C) a wide slab ($W = 7,000 \text{ km}$). Subduction is driven by buoyancy forces only, reflecting natural subduction systems. The grey color indicates the top of the lower mantle. Note that the narrow and intermediate width slabs are characterized by trench retreat and slab rollback, while the wide slab is characterized by an approximately stationary trench in the center (at the symmetry plane) but trench retreat and slab rollback near the slab edge.

Table S1. Model set-up.

Experiment	W/T_{UM}	W (km)	box width (km)	box length (km)
4L-1	0.45	300	14,000	7,000
4L-2	0.91	600	14,000	7,000
4L-3	1.36	900	14,000	7,000
4L-4	1.82	1,200	14,000	7,000
4L-5	2.27	1,500	14,000	7,000
4L-6	3.03	2,000	14,000	7,000
4L-7	4.55	3,000	14,000	7,000
4L-8	6.06	4,000	14,000	7,000
4L-9	7.58	5,000	14,000	7,000
4L-10	9.09	6,000	14,000	7,000
4L-11	10.61	7,000	14,000	7,000

Table S1. Values for slab width (W) and box dimensions for the numerical simulations. Plate thickness is 100 km. Box depth is 1,000 km. Separation between trailing edge and back wall is 1,300 km. Transition zone is at 660 km. T_{UM} is upper mantle thickness (660 km). Note that numerical models were run with the full box length but only half the box width due to the symmetry of the problem along the mid-plane (see Methods section 1.1 and Figure S1).

References

- S1. D. R. Stegman, J. Freeman, W. P. Schellart, L. Moresi, D. May, *Geochemistry Geophysics Geosystems* **7**, Q03012 (2006).
- S2. L. Moresi, F. Dufour, H.-B. Mühlhaus, *Journal of Computational Physics* **184**, 476 (2003).
- S3. W. P. Schellart, J. Freeman, D. R. Stegman, L. Moresi, D. May, *Nature* **446**, 308 (2007).
- S4. F. A. Capitanio, G. Morra, S. Goes, *Earth and Planetary Science Letters* **262**, 284 (2007).
- S5. F. A. Capitanio, G. Morra, S. Goes, *Geochemistry Geophysics Geosystems* **10**, Q04002 (2009).
- S6. M. OzBench *et al.*, *Physics of the Earth and Planetary Interiors* **171**, 224 (2008).
- S7. L. Moresi, M. Gurnis, *Earth and Planetary Science Letters* **138**, 15 (1996).
- S8. M. Billen, M. Gurnis, M. Simons, *Geophysical Journal International* **153**, 359 (2003).
- S9. W. P. Schellart, *Geochemistry Geophysics Geosystems* **9**, Q03014 (2008).
- S10. F. Funiciello *et al.*, *Earth and Planetary Science Letters* **271**, 233 (2008).
- S11. B. Wu, C. P. Conrad, A. Heuret, C. Lithgow-Bertelloni, S. Lallemand, *Earth and Planetary Science Letters* **272**, 412 (2008).
- S12. C. Loiselet, L. Husson, J. Braun, *Geology* **37**, 747 (2009).
- S13. W. P. Schellart, *Earth and Planetary Science Letters* **288**, 309 (2009).
- S14. D. R. Stegman, R. Farrington, F. A. Capitanio, W. P. Schellart, *Tectonophysics* **483**, 29 (2010).
- S15. L. Moresi, V. Solomatov, *Geophysical Journal International* **133**, 669 (1998).
- S16. W. P. Schellart, *Journal of Geophysical Research* **109**, B07401 (2004).
- S17. F. Funiciello, C. Faccenna, D. Giardini, *Geophysical Journal International*, doi:10.1111/j.1365 (2004).
- S18. S. Goes, F. A. Capitanio, G. Morra, *Nature* **451**, 981 (2008).
- S19. W. P. Schellart, *Physics of the Earth and Planetary Interiors* **170**, 73 (2008).
- S20. M. E. Magee, M. D. Zoback, *Geology* **21**, 809 (1993).
- S21. K. Wang, T. Mulder, G. C. Rogers, R. D. Hyndman, *Journal of Geophysical Research* **100**, 12907 (1995).
- S22. K. Wang, Y. Hu, *Journal of Geophysical Research* **111**, B06410 (2006).
- S23. M. Cloos, *Geological Society of America Bulletin* **105**, 715 (1993).
- S24. J. C. Afonso, G. Ranalli, M. Fernández, *Geophysical Research Letters* **34**, L10302 (2007).
- S25. C. Kincaid, P. Olson, *Journal of Geophysical Research* **92**, 13 (1987).
- S26. B. H. Hager, *Journal of Geophysical Research* **89**, 6003 (1984).
- S27. G. Kaufmann, K. Lambeck, *Physics of the Earth and Planetary Interiors* **121**, 301 (2000).
- S28. Y. Torii, S. Yoshioka, *Tectonophysics* **445**, 200 (2007).
- S29. J. Ganguly, A. M. Freed, S. K. Saxena, *Physics of the Earth and Planetary Interiors* **172**, 257 (2009).
- S30. W. P. Schellart, D. R. Stegman, J. Freeman, *Earth-Science Reviews* **88**, 118 (2008).
- S31. W. P. Schellart, *Geological Society of America Bulletin* **120**, 1441 (2008).
- S32. P. Clift, P. Vannucchi, *Reviews of Geophysics* **42**, RG2001 (2004).
- S33. C. O'Neill, D. Müller, B. Steinberger, *Geochemistry Geophysics Geosystems* **6**, Q04003 (2005).
- S34. T. W. Becker, *Geophysical Research Letters* **35**, L05303 (2008).
- S35. R. D. Müller, W. R. Roest, *Journal of Geophysical Research* **97**, 3337 (1992).
- S36. R. G. Gordon, D. M. Jurdy, *Journal of Geophysical Research* **91**, 12389 (1986).
- S37. D. F. Argus, R. G. Gordon, *Geophysical Research Letters* **18**, 2039 (1991).
- S38. C. Kreemer, W. E. Holt, A. J. Haines, *Geophysical Journal International* **154**, 8 (2003).
- S39. P. Wessel, Y. Harada, L. W. Kroenke, *Geochemistry Geophysics Geosystems* **7**, Q03L12 (2006).
- S40. C. DeMets, R. G. Gordon, D. F. Argus, S. Stein, *Geophysical Research Letters* **21**, 2191 (1994).
- S41. P. Bird, *Geochemistry Geophysics Geosystems* **4**, 1027 (2003).
- S42. R. D. Müller, M. Sdrolias, C. Gaina, B. Steinberger, C. Heine, *Science* **319**, 1357 (2008).
- S43. R. C. Kerr, J. R. Lister, *J. Geol.* **99**, 457-467 (1991).
- S44. T. Atwater, *GSA-Bulletin* **81**, 3513-3536 (1970).
- S45. P. G. DeCelles, *American Journal of Science* **304**, 105 (2004).
- S46. L. J. Sonder, C. H. Jones, *Annual Review of Earth and Planetary Sciences* **27**, 417 (1999).
- S47. R. R. Parrish, S. D. Carr, D. L. Parkinson, *Tectonics* **7**, 181 (1988).
- S48. O. Oncken *et al.*, in *The Andes - Active Subduction Orogeny* O. Oncken *et al.*, Eds. (Springer, 2007) pp. 3-27.
- S49. C. D. Henry, J. J. Aranda-Gomez, *Geology* **20**, 701 (1992).
- S50. D. S. Wilson, *Journal of Geophysical Research* **98**, 16053 (1993).